

# Rational Integration of Inbuilt Aperture with Mesoporous Framework in Unusual Asymmetrical Yolk–Shell Structures for Energy Storage and Conversion

Ting Zhu,<sup>†</sup> Liangliang Zhu,<sup>†</sup> Jing Wang,<sup>†</sup> and Ghim Wei Ho<sup>\*,†,‡,§</sup>

<sup>†</sup>Department of Electrical and Computer Engineering, National University of Singapore, 4 Engineering Drive 3, Singapore 117583

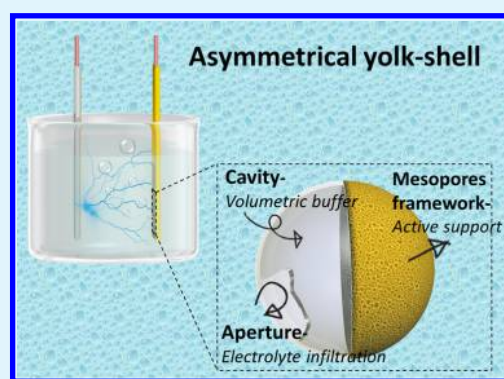
<sup>‡</sup>Engineering Science Programme, National University of Singapore, 9 Engineering Drive 1, Singapore 117575

<sup>§</sup>Institute of Materials Research and Engineering, A\*STAR (Agency for Science, Technology and Research), 3 Research Link, Singapore 117602

## Supporting Information

**ABSTRACT:** Despite the attractive benefits of hollow structures as electrodes for advanced energy storage–conversion capabilities, one prevailing shortcoming is their compromised structural integrity and volumetric energy density due to the introduction of an ultrathin shell with an excessively underutilized large hollow cavity. Herein, we report a facile and template-free synthetic route to realize unusual asymmetrical yolk–shell (AYs) structures composed of mixed-valence  $\text{NiCo}_2\text{O}_4$  material. Explicitly, this work highlights the unusual off-central core, an AYs structure that encompasses a hemispherical hollow interior, and a mesoporous solid counterpart. As such, it retains desirable hollow structural characteristics while favorably precludes the excessive unexploited hollow interior space for increased active material packing. Unlike the conventional symmetrical yolk–shell (SYs) which is composed of a porous shell framework radially throughout the structure, the mesoporous solid constitution of the AYs structure offers an inbuilt reinforced framework to support the partial porous shell and concurrently leaves sufficient void for volumetric buffering. Another unique structural feature of the AYs structure is the formation of a submicron aperture or opening on the shell that enhances accessibility of electrolyte diffusion. All of these synergistic structural features of  $\text{NiCo}_2\text{O}_4$  AYs structures enhance the pseudocapacitive and electrocatalytic properties.

**KEYWORDS:** yolk–shell, mesoporous,  $\text{NiCo}_2\text{O}_4$ , supercapacitor, oxygen evolution reaction OER



## 1. INTRODUCTION

With increasing demand for clean and sustainable energy, immense research is focused on advancing pseudocapacitive and electrocatalytic energy storage–conversion capabilities.<sup>1–5</sup> Generally, the selection of a pertinent active electrode material for pseudocapacitive and electrocatalytic properties involves compromising adaptation of electrochemical reactivity, thermodynamic stability, corrosion resistance, materials, and manufacturability cost factors.<sup>6,7</sup> By and large, these essential characteristics can be optimized through structural and compositional tuning. Accordingly, structural tuning modulates the accessibility of active sites for ion transportation, while compositional variation correlates to the electronic state, which affects the strength of surface intermediate bonds and hence its electrochemical reactivity. Among the explored low-cost and earth abundance transition metal oxides (TMOs), spinel type  $\text{Co}_3\text{O}_4$  has been intensely studied for electrochemical energy storage and conversion, such as water oxidation/oxygen evolution reaction (OER), due to its highly reversible surface redox reactions, superior catalytic properties, and high corrosion durability.<sup>8–10</sup> Nonetheless, the electrochemical

performances of  $\text{Co}_3\text{O}_4$  are still limited by its simplistic binary composition. To improve its electrochemical activity, Ni atoms have been intentionally incorporated to form ternary nickel cobaltite ( $\text{NiCo}_2\text{O}_4$ ), a mixed-valence oxide which has proven to enhance the electrical conductivity and electrochemical catalytic active sites.<sup>11–13</sup>

In regards to structural tuning, the performances of electrode materials are often limited by poor structural integrity and low active material content. Correspondingly, these limitations lead to prevalent mechanical fracturing during prolong cycling as well as volumetric energy density inadequacies. As such, structural tuning strategies to counteract these constraints are highly desired to further improve the electrochemical performances. It has been proven that porous hollow structures possess many intriguing characteristics such as high surface area with abundant reactive sites and shell permeability with facilitated ion diffusion.<sup>14–18</sup> In spite of the aforementioned benefits, its

**Received:** September 27, 2016

**Accepted:** November 10, 2016

**Published:** November 10, 2016

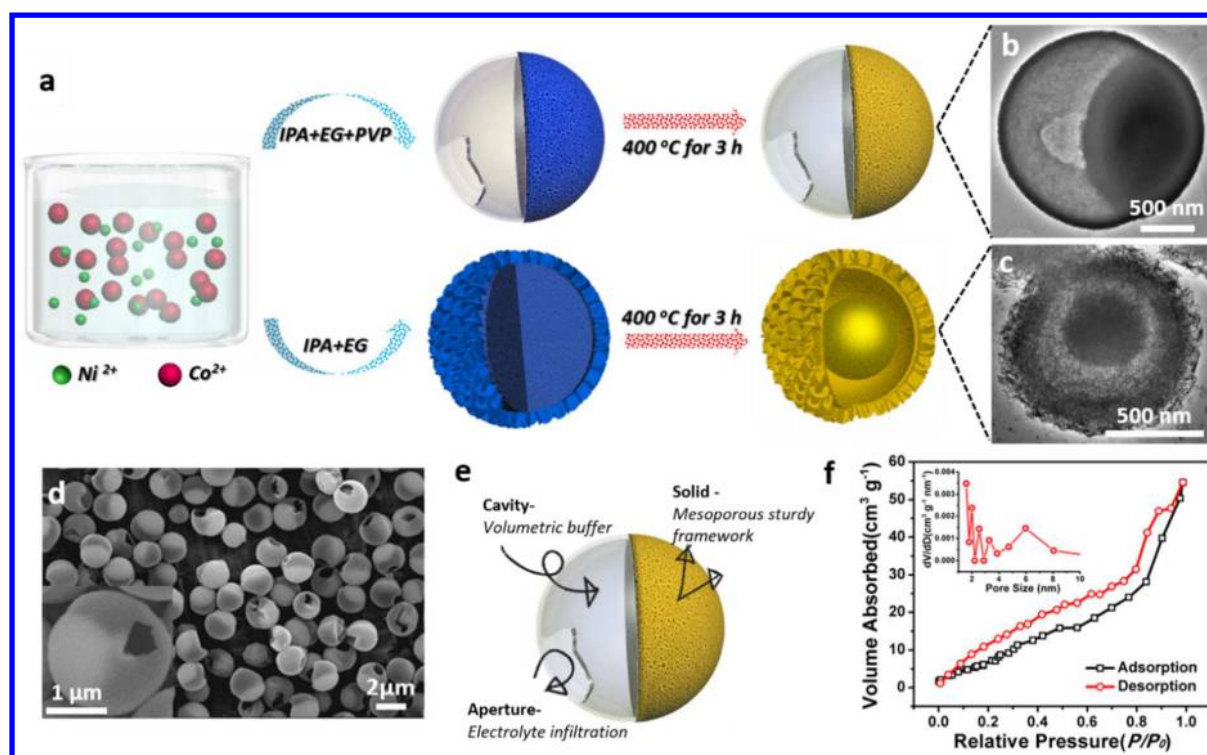


**Figure 1.** Schematic process flow of both AYs and SYs structures (a). TEM images (b and c) of the derived AYs (b) and SYs (c)  $\text{NiCo}_2\text{O}_4$  spheres. SEM image (d) of the AYs  $\text{NiCo}_2\text{O}_4$  spheres with inset showing a higher magnification. Conceptual design with structural features (e) and BET surface area and pore size (inset) of the AYs structure (f).

prevalent shortcomings manifest as compromised structural integrity and impoverished volumetric energy density due to the introduction of an ultrathin shell with an excessively unused large hollow cavity. To extend to the underutilized large empty spaces of a hollow cavity, hierarchical hollow structures such as yolk–shell spheres have been synthesized to better utilize or exploit the hollow interior.<sup>19–25</sup> Thus far, the synthesized yolk–shell spheres are predominantly symmetrical in shape, while homogeneous formation of AYs structures with an off-central core displacement is rarely seen. Moreover, developing a facile and template-less synthetic route to realize controllable formation of AYs hollow structures of mixed-valence oxide compositions still remains a huge challenge and not reported to date.

Herein, we have devised a facile, template-free synthetic route that has enabled manipulation of unusual AYs spheres with a combined inbuilt aperture and mesoporous framework. Particularly, this work highlights the formation of AYs spheres as it notably encompasses a partial hollow interior and a partial mesoporous solid counterpart. The asymmetrical structure preserves favorable hollow structural characteristics and at the same time optimizes the exploitation of the excessive hollow interior space/cavity. The exceptional inbuilt mesoporous solid constitution offers additional benefits such as a sturdy framework that reinforces the ultrathin porous shell and higher active material content for respective volumetric buffering and energy conversion efficiency. Another unique structural feature is the formation of a submicron aperture or opening on the shell of the AYs sphere that enhances accessibility of electrolyte diffusion. All of these synergistically designed structural and compositional features of the AYs structures translate into superior energy storage and conversion properties in pseudocapacitors and electrocatalysis for water splitting.

## 2. RESULTS AND DISCUSSION

A straightforward and template-free synthetic route is employed to configure two distinct yolk–shell architectures, namely, unique AYs and common SYs. The synthesis process flow of two variable nickel cobalt precursors and subsequent oxides yolk–shell structures is schematically shown in Figure 1a. For the formation of the typical AYs sample, the introduction of 0.1 g of polyvinylpyrrolidone (PVP) and 1 mL of ethylene glycol (EG) into the synthesis produced a precursor with AYs spheres. The  $\text{Ni}^{2+}$  and  $\text{Co}^{2+}$  are affinitive to EG molecules to form a glycolate complex, which has been widely reported elsewhere.<sup>26</sup> The PVP herein may have played as an important capping reagent at the interface between the metal ions and EG molecules, which then slowed and limited the growing procedure.<sup>27</sup> In addition, the presence of PVP could be vital for the morphological evolution of the Ni-Co precursors. Our control experiments have shown that closed spheres with a rough surface will be obtained when 0.05 g of PVP is used, but no precipitates can be collected if 0.5 g of PVP is applied. It should be noted that the amount of PVP (0.1 g) in this work is an optimized dosage, which ensured the robust shell structures of the particles with a hollow interior as large as possible (Figure S1a). In addition, the shell has been partially dissolved by PVP to create a cavity which could serve as a gateway for the electrolyte diffusion. As a comparison, SYs spheres with nanosheets are also prepared by the same procedure only in the absence of PVP (Figure S1b). It should also be noted that the formation of AYs and SYs is highly dependent on the solvent used. Usage of ethanol instead of IPA will lead to distinct morphological changes, though other conditions are unaltered (Figure S9). The as-synthesized AYs and SYs precursors were analyzed by EDX (Figure S1c) and XRD (Figure S1d), which reveals the formation of an amorphous Ni-

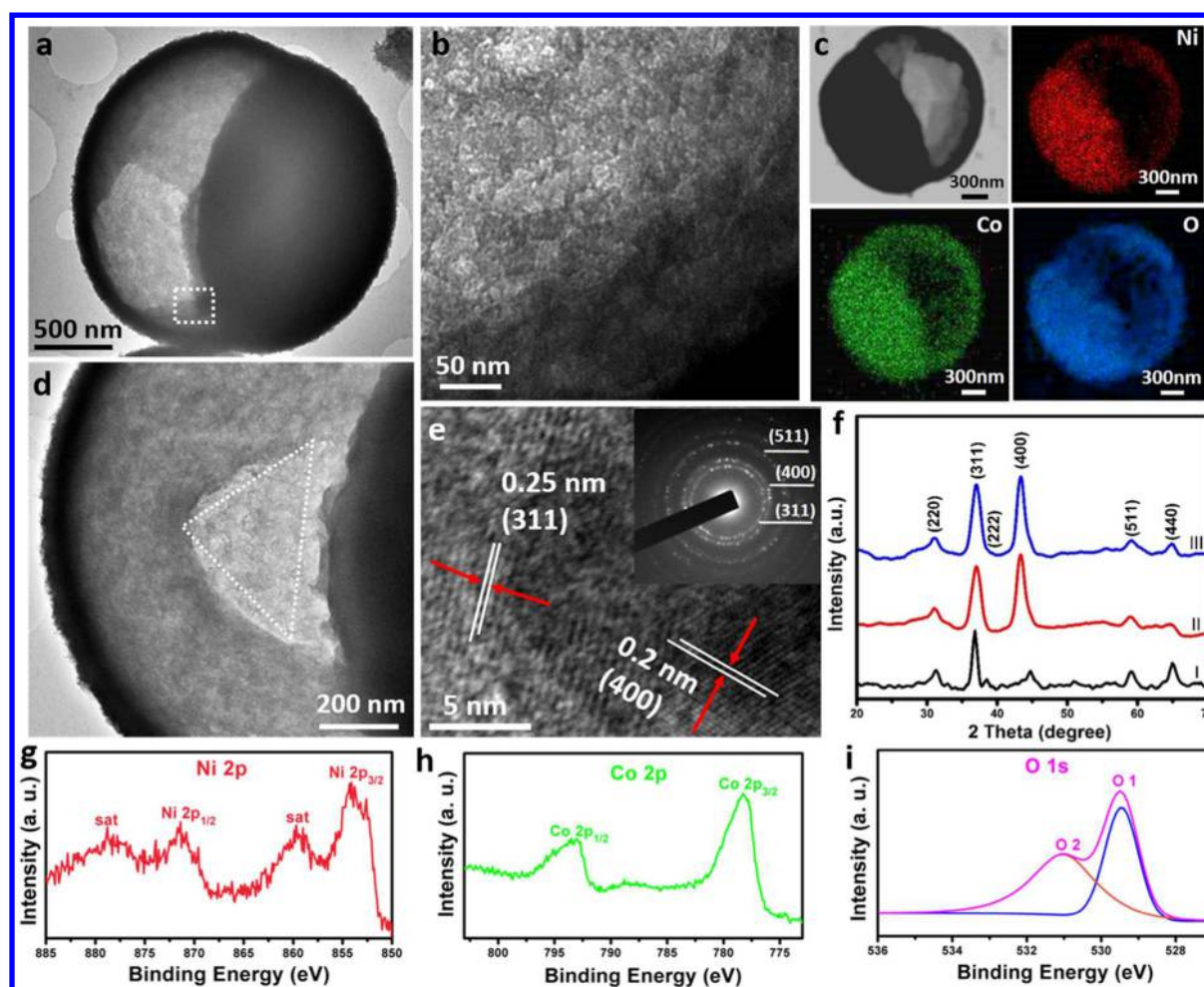


**Figure 2.** TEM (a, b, d), elemental mapping (c), HR-TEM (e), and XPS results (g–i) of the AYs structure. XRD spectra (f) of control sample (I), AYs (II), and SYs (III).

Co complex. The subsequent heat treatment at 400 °C for 3 h in air has converted the as-formed precursors (both AYs and SYs) to the corresponding oxides, whose shapes can be retained after the heat treatment, revealing the structural stability of the particles (Figure 1b,c). The weight loss of the precursors during the combustion was also monitored by TGA (Figure S2). The initial weight loss within 100 °C for both of the samples was probably caused by the evaporation of water content absorbed in the sample powder. A higher mass loss was observed for AYs than that of SYs (200–250 °C), which could be due to the combustion of the additional PVP residue contained in AYs.<sup>28</sup> It also can be seen that the weight curve is stable when the temperature reaches 400 °C, confirming the complete combustion of the organic species and conversion to oxides at this temperature. On the basis of our results, a higher annealing temperature at 500 °C (Figure S10b) will lead to deformation of AYs particles and collapse of the inbuilt apertures, indicating that a proper annealing temperature should be used to preserve the structural features.

The formation of the core–shell structure of the SYs sample could be induced by the Kirkendall effect, by which Ni and Co species traveled outward at different diffusion rates, leading to the formation of symmetrical core–shell structures.<sup>29</sup> Different from the SYs sample, the AYs structure has been formed during the solvothermal process in the presence of both EG and PVP. The EG molecules served as soft templates for the assembly of

metal ions and facilitated the subsequent growth of the Ni-Co precursor, while the PVP may have played a role as capping reagent, which restricted the fast growth of the Ni-Co precursor or even dissolved the as-formed structure. As a result, AYs structures with an aperture inbuilt on the thin shells (where Ni-Co species dissolved locally) were formed by the effect of PVP and EG. Time-dependent experiments (2, 4, 8 h) were carried out to examine any changes of core size in the AYs structures. The SEM results are shown as Figure S11, where no distinct changes of core sizes can be observed when the reaction time is 2, 4, and 8 h compared to the typical 6 h. However, some nanoparticles are observed at 8 h, which could be due to gradual dissolution of the precursor. It is worthy to mention that no precipitates were collected after experiments, no matter whether the reaction time was 2, 4, 6, or 8 h if 0.5 g of PVP was used, which shows that excess PVP present in the solution will prevent the formation of the Ni-Co precursor.

The as-derived AYs oxide particles are monodispersed and fairly uniform in size  $\sim 2 \mu\text{m}$  in diameter (Figure 1d). A distinct contrast of the two halves (semihollow–semisolid) in asymmetrical spherical structures can be observed in Figure 1d, inset. Interestingly, the AYs sphere presents a segmented structure consisting of two halves: one part of a hollow interior and the other a mesoporous solid counterpart. Figure 1e highlights the conceptual design of the atypical AYs structure which not only preserves the general favorable hollow structural characteristics

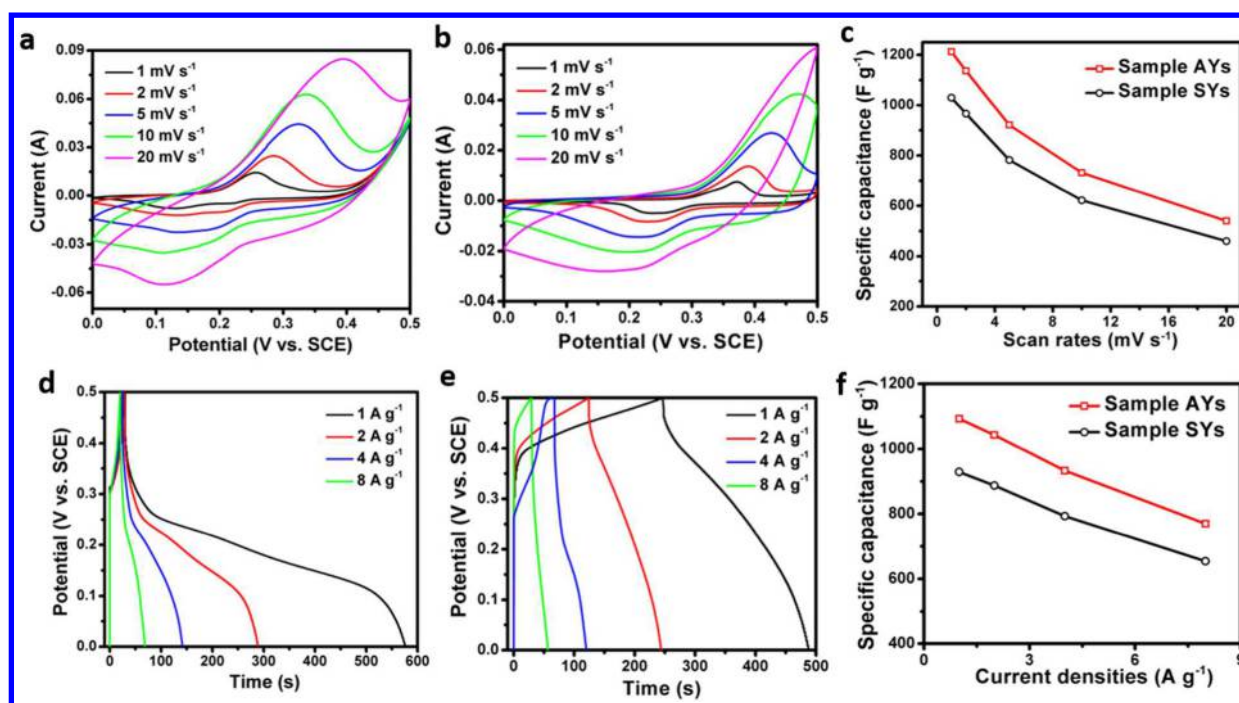


**Figure 3.** CV curves (a and b) of AYs (a) and SYs (b) structures; capacitances calculated from CV curves of both yolk–shell samples (c); GCCD curves (d and e) of AYs (d) and SYs (e) structures; and capacitances calculated from GCCD curves of both yolk–shell samples (f).

but also reduces the excessive unexploited hollow interior space/cavity. The inbuilt mesoporous solid constitution offers additional attributes such as a self-supported framework to reinforce the thin porous shell and a higher active material content essential for volumetric buffering. Additionally, the exclusive formation of the submicron aperture or opening on its shell enhances the accessibility of electrolyte diffusion and eases bubble evolution for the electrochemical process. It is noteworthy that, simply by PVP exclusion, the morphology evolves into a SYs sphere with a porous sheetlike shell and entrapped core after the annealing process (Figure S3a). In view of the electrochemical and catalytic reactivity kinetically controlled by the ion adsorption–diffusion, surface areas and pore sizes of the both yolk–shell structures were determined by BET. The  $N_2$  adsorption–desorption isotherms and the corresponding Barrett–Joyner–Halenda (BJH) pore size distributions (inset) of AYs and SYs structures are shown in Figure 1f and Figure S3d, respectively. The isotherms can be categorized as type IV, which signifies typical mesoporous structures of the AYs ( $SSA = 36 \text{ m}^2 \text{ g}^{-1}$ ) and SYs ( $SSA = 61 \text{ m}^2 \text{ g}^{-1}$ ) structures with pore diameters ranging from 3 to 12 nm. The higher surface area of the SYs structures can be attributed to the presence of densely packed sheetlike structures (Figure S3a). Despite the AYs structure having a smaller surface area than the SYs one, it is noteworthy the surface area is not the predominant factor that affects the electrochemical performances (to be discussed later).

Under TEM observation of sample AYs, an asymmetrical yolk–shell structure with an average diameter of  $\sim 2 \mu\text{m}$  can be seen (Figure 2a). At higher magnification of the marked area, pores and voids can be observed, indicating that the AYs (both hollow and solid parts) is composed of a porous structure (Figure 2b). The inbuilt aperture of the AYs structure is highlighted by a TEM image in Figure 2d (marked by the white triangle), which is designed as an efficient pathway for the transportation of electrolyte. Additional HR-TEM character-

izations with the SAED pattern were carried out where lattice spacings of 0.2 and 0.25 nm corresponding to (400) and (311) facets of  $\text{NiCo}_2\text{O}_4$  have been detected for the AYs structure, which can be further confirmed with the SAED patterns (Figure 2e and inset).

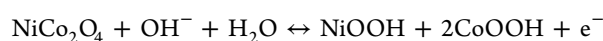
TEM characterizations were also performed for the SYs structure, which show densely packed nanosheets structures (Figure S3a). Similarly, the (400) plane along with the (220) plane can be identified (Figure S3b). The elemental mappings for both of the yolk–shell samples are performed to elucidate the compositional distributions (Figure 2c and Figure S3c). The elements Ni, Co, and O are observed to be homogeneously distributed throughout the structure, which suggests uniform formation of  $\text{NiCo}_2\text{O}_4$  yolk–shell structures.

In order to obtain more crystallographic details, the yolk–shell structures are examined by XRD (Figure 2f). All the indexed peaks can be attributed to (220), (311), (222), (400), (511), and (440) planes of the cubic  $\text{NiCo}_2\text{O}_4$  (JCPDS 20-0781).<sup>30</sup> No impurities peak has been found, which reveals a complete conversion of nickel cobalt precursor structures into  $\text{NiCo}_2\text{O}_4$ . It should be noted that, in contrast to the control  $\text{NiCo}_2\text{O}_4$  nanoparticles sample prepared without EG or PVP (Figure S4a,b), both yolk–shell structures exhibit an intense (400) diffraction peak, showing their unusual highly exposed (400) facet. This finding is consistent with the HR-TEM observations. In general, the high index facet possesses increased surface energy, hence rendering more active sites for electrochemical activity.<sup>31</sup> The chemical compositions of the typical AYs sample are further analyzed by XPS. The Ni 2p spectrum (Figure 2g) contains two prominent  $2p_{3/2}$  and  $2p_{1/2}$  spin–orbit peaks at binding energies of 853.2 and 872.4 eV with two shakeup satellites (marked as “sat”). Two distinct peaks at binding energies of 779.5 and 795.6 eV are observed for the Co 2p, corresponding to the Co  $2p_{3/2}$  and Co  $2p_{1/2}$ , respectively (Figure 2h). The high-resolution spectrum for the O 1s (Figure 2i) indicates two main oxygen contributions,

which are marked as O1 and O2, respectively. The O1 at 529.3 eV and O2 at 531.2 eV are attributed to the metal oxygen bonds and oxygen ions, respectively. These results have confirmed that the surface of the asymmetrical NiCo<sub>2</sub>O<sub>4</sub> sample has a composition of Ni<sup>2+</sup>, Ni<sup>3+</sup>, Co<sup>2+</sup>, and Co<sup>3+</sup>.<sup>32,33</sup>

The overall structures are well-retained after the heat treatment, revealing their structural stability characteristics. The various morphologies derived from the final products results from the coeffects of solvents and surfactants. It is plausible that the EG serves as a soft scaffold for the nucleation of metal ions, while PVP limits the growth of a specific crystal direction, which leads to formation of a mesopores structure.<sup>34</sup> Remarkably, the eventual SYs structure could be attributed to the Kirkendall effect where Ni and Co atoms diffused outward at different rates occurring during the thermal oxidation process.<sup>35,36</sup>

The as-prepared NiCo<sub>2</sub>O<sub>4</sub> yolk–shell structures are then evaluated as electrode materials for supercapacitors. Figure 3a,b illustrates the CV curves performed for AYs and SYs structures at different scan rates (1, 2, 5, 10, 20 mV s<sup>-1</sup>) with a potential window ranging from 0 to 0.5 V (vs SCE). Distinct redox peaks occur at 0.1–0.25 V and 0.3–0.45 V, which reveal the pseudocapacitive characteristics of the electrodes. The different CV shapes of the two samples can be attributed to the different extent of polarization of the electrode materials.<sup>37</sup> The relevant redox reactions can be described by the following equation:<sup>3,38,39</sup>



The specific capacitances of all the samples can be calculated by the following equation

$$C = \frac{1}{2m \frac{dV}{dt} (V_a - V_b)} \int_{V_b}^{V_a} I(V) dV$$

where  $m$  is the active material mass,  $\frac{dV}{dt}$  is the scan rate,  $V_a - V_b$  represents the potential window which is 0.5 V, and the last integral term is the area bounded by the CV curves.<sup>40</sup> Figure 3c shows the comparison of specific capacitance of both yolk–shell structures at different scan rates. The AYs sample shows high specific capacitances of 1212, 1136, 921, 732, and 540 F g<sup>-1</sup> at scan rates of 1, 2, 5, 10, and 20 mV s<sup>-1</sup>, respectively while the SYs one exhibits corresponding lower capacitances of 1030, 966, 782, 622, and 460 F g<sup>-1</sup>. The galvanostatic charge–discharge is also conducted at various current densities within the same potential window for both samples (Figure 3d,e), which reaffirms the Faradaic characteristics of the two samples. The specific capacitances delivered at different current densities (1, 2, 4, and 8 A g<sup>-1</sup>) are shown in Figure 3f. The highest specific capacitance can be delivered by the AYs at a current density of 1 A g<sup>-1</sup> (1093 F g<sup>-1</sup>), while a lower capacitance of 929 F g<sup>-1</sup> is recorded at the same current density for SYs. High capacitances of 770 and 654 F g<sup>-1</sup> can be retained at a high current density of 8 A g<sup>-1</sup> for AYs and SYs, respectively. As a comparison, the CV and GCCD measurements were also carried out for the NiCo<sub>2</sub>O<sub>4</sub> solid nanoparticles (control sample) (Figure S5a–c). The shapes of CV and GCCD curves are very similar to the yolk–shell structures, but at much lower specific capacitances of 580, 365, 218, and 110 F g<sup>-1</sup> at the same current densities of 1, 2, 4, and 8 A g<sup>-1</sup>, respectively. Both yolk–shell structures impart superior electrochemical performances compared to the NiCo<sub>2</sub>O<sub>4</sub> nanoparticles owing to the desirable porous and hollow structural features. Though both

yolk–shell structures deliver competitive electrochemical performances, the AYs structure outperforms the conventional SYs structure. This possibly stems from its defining advantages of an asymmetrical structure that not only retains favorable hollow structural characteristics but also at the same time utilizes the excessive hollow interior cavity for higher active material content. Another distinctive structural feature is the formation of the submicron aperture or opening on the shell which may facilitate the electrolyte ion transportation. As a further insight of full-cell supercapacitors, an asymmetrical two-electrode system was fabricated to evaluate the electrochemical performances for the typical AYs sample (Figure S12). Distinct redox peaks can be clearly seen from the CV results, revealing the high electroactivity of the active materials (Figure S12a). Specific capacitances of the two-electrode system were calculated following a previous report, where the values were derived based on the total mass of two electrode active materials.<sup>41</sup> As a result, capacitances of 110.8–44 F g<sup>-1</sup> can be delivered at current densities of 0.125–1 A g<sup>-1</sup>, which were calculated from discharge curves of the GCCD results (Figure S12b,c).

The electrical conductivities of the NiCo<sub>2</sub>O<sub>4</sub> yolk–shell structures are evaluated using EIS. The Nyquist plots are presented in Figure 4a with an inset showing the details of the high-frequency region. The first intersections of the Nyquist

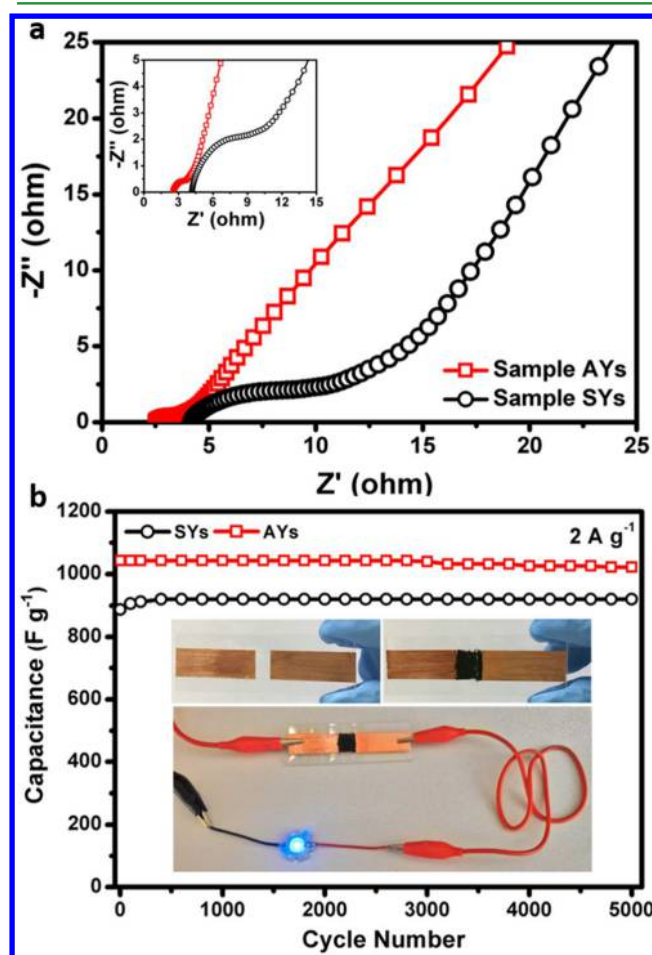


**Figure 4.** EIS (a) with an inset showing high magnification of high-frequency region of the Nyquist plots and cycling performances (b) of AYs and SYs structures. The insets in (b) show electrical conductivity demonstration of AYs structure.

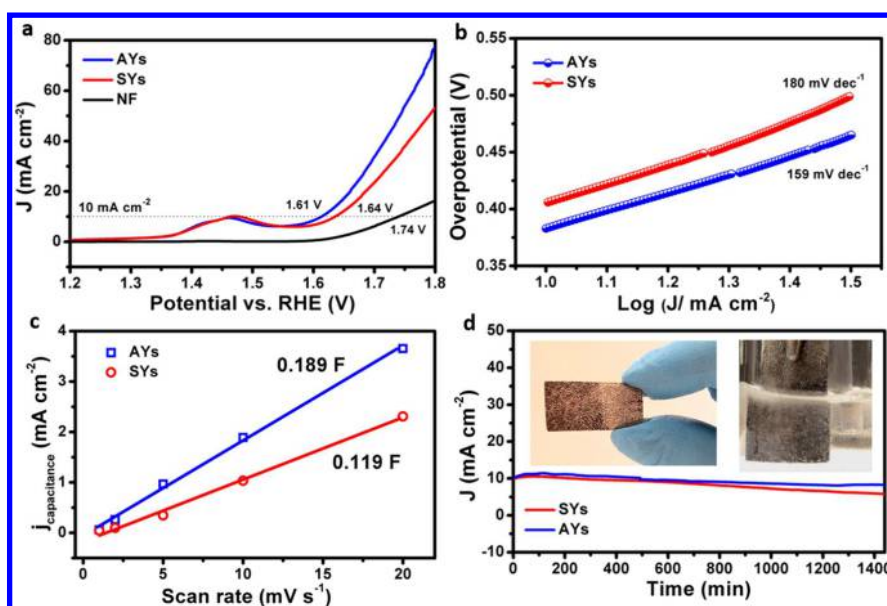


**Figure 5.** Polarization curves (a), Tafel plots (b), capacitances (c) calculated from non-Faradaic region of CV curves (0–0.02 V vs SCE), and stability performances (d) of AYs and SYs  $\text{NiCo}_2\text{O}_4$  electrodes for OER.

plots on the  $Z'$  axis in the high-frequency region reveal the high-frequency equivalent series resistance of capacitors ( $R_s$ ) which are contributed by the Ohmic resistance of the electrolyte, the internal resistance of the electrode materials, and contact resistance between electrodes and current collectors.<sup>5</sup> Meanwhile, the semicircles crossing high and mid-frequency can be attributed to the charge-transfer resistance (magnified in the inset). It is derived from the EIS that the AYs structure exhibits lower charge-transfer impedance and better electrical conductivity than that of SYs due to the observed lower  $R_s$  value and smaller radius of the semicircle. However, both of the yolk–shell samples have shown better EIS performances than that of the controlled  $\text{NiCo}_2\text{O}_4$  nanoparticle (Figure S5d).

Furthermore, the electrical conductivities of both yolk–shell structures are ascertained through simple demonstration. The  $\text{NiCo}_2\text{O}_4$  yolk–shell materials were dispersed in pure ethanol to form a homogeneous slurry before applying onto glass slides to physically connect two preattached copper films. The copper/slurry/copper attached glass slides were dried in an oven and then connected to an LED to form a close circuit with an external power supply. The LED can be powered when a potential of 3.7 V was applied, revealing a good electrical conductivity of the asymmetrical yolk–shell structure (Figure 4b, insets). Similarly good electrical conductivity is attested for the SYs structure (photos not shown). In contrast, the control  $\text{NiCo}_2\text{O}_4$  nanoparticles sample displays a dimly lighted LED at the same voltage, showing its relatively poorer conductivity (Figure S6).

Both AYs and SYs of  $\text{NiCo}_2\text{O}_4$  electrodes are also tested for prolonged cycling to evaluate the stability at a current density of  $2 \text{ A g}^{-1}$  (Figure 4b). There is no distinct capacitance decay for both of the samples, i.e.,  $>1000 \text{ F g}^{-1}$  for AYs and  $>900 \text{ F g}^{-1}$  for SYs after 5000 cycles. These observations can be credited to good cycling capabilities of both yolk–shell structures. It is apparent that a slight increase of the capacitance in the first few hundreds cycles can be detected only for the SYs sample. This modest increase in capacitance can be attributed to the slower electrode activation process since electrolyte ions

may take a longer time to diffuse into the interior of the inherently thicker shell and aperture-less SYs spheres. On the contrary, the redox kinetics is anticipated to be much faster for the AYs structure since the infiltration of electrolyte through the readily available opening presents a much lower permeation barrier. It should also be noted that the Ni foam templates contribute  $\sim 1\%$  of the total capacitances of all the samples according to our control experiment. This means that the measured capacitances are largely delivered by the electroactive yolk–shell nanostructured materials. The morphology of the electrode materials (AYs and SYs) cycled for 5000 cycles is also examined by SEM (Figure S7). It is clearly seen that the structures of both AYs and SYs particles can be retained after prolonged cycles, showing their good structural stabilities (the small nanoparticles observed in SEM images are carbon black that is used as conductive reagent for the electrodes). The high specific capacitances with excellent cycling performances reported herein are comparable to some of the previous work listed in Table S1.

The electrocatalytic properties for OER have also been evaluated for the as-prepared yolk–shell  $\text{NiCo}_2\text{O}_4$  samples. Figure 5a shows the polarization curves of yolk–shell samples and pure nickel foam. The SYs structure delivers a current density of  $10 \text{ mA cm}^{-2}$  at a potential of 1.64 V (vs RHE), whereas a lower potential of 1.61 V (vs RHE) only is required for the AYs structure to deliver the same current density. One may recall that a higher surface area of sample SYs than AYs is reported in this work, which could bring about a better electrochemical performance for SYs. Nevertheless, it should be noted that the SYs sphere is a relatively closed system, which may result in a slower kinetic of mass transportation, hence possibly leading to a compromised catalytic performance. For the pure nickel foam (NF), it is observed that the current density does not reach  $10 \text{ mA cm}^{-2}$  unless a much higher potential of 1.74 V (vs RHE) is applied. The LSV was also conducted for the solid  $\text{NiCo}_2\text{O}_4$  particles (control sample), and a higher overpotential of 1.71 V (vs RHE) was observed (Figure S8). The OER kinetics of these two electrodes are further estimated by the Tafel plots. As shown in Figure 5b, the

Tafel slope of the AYs is  $159 \text{ mV dec}^{-1}$  compared to SYs of  $180 \text{ mV dec}^{-1}$ , which are comparable to some of the previous work.<sup>42,43</sup> In order to further explain a better OER performance of AYs, electrochemically active surface areas (ECSA) were estimated for both of the yolk–shell samples by calculation of electrochemical double-layer capacitance of the catalytic surface.<sup>44</sup> The capacitances of both of the samples shown in Figure 5c were calculated from a non-Faradaic CV region (0–0.02 V vs SCE) where a higher capacitance of 0.189 F can be obtained for AYs compared to SYs (0.119 F). This result reveals a higher ECSA of AYs, which reconfirms its better OER performance even though the specific surface area is smaller than that of SYs.

Besides the catalytic activity, current stabilities of the yolk–shell structures at fixed overpotentials (380 mV for AYs and 410 mV for SYs) were monitored up to 1440 min (Figure 5d). Figure 5d insets show the active yolk–shell structures loaded nickel foam and evolution of gas bubbles during the OER measurement. Both of the samples have shown good cycling stability after 720 min, where a retention of 88% can be obtained for AYs compared to 81% for SYs). Even after a prolonged time to 1440 min, 79% of the current can be retained for AYs, whereas a lower retention of 55% only is preserved for SYs. The OER performances presented in this work are comparable to some of the relevant work listed in Table S2. As a whole, the superior electrochemical performances in terms of supercapacitors and oxygen evolution may be largely attributed to the high conductive mixed-valence ternary materials with integrated robust yolk–shell structural architectures. The physical surface area plays an important role in the electrochemical process, but not the dominant factor, while the ECSA could be more significant to the electrochemical performance. The reported yolk–shell  $\text{NiCo}_2\text{O}_4$  materials in this work may be potential candidates in the next-generation energy storage and conversion applications.

### 3. CONCLUSIONS

A template-free solution-based preparation method has been developed to realize two distinctive yolk–shell architectures, i.e., AYs and SYs spheres of mixed-valence  $\text{NiCo}_2\text{O}_4$ . The unusual AYs spheres composed of a partial hollow interior and a partial mesoporous solid counterpart have shown to preserve beneficial hollow structural characteristics and at the same time optimize the exploitation of the excessive hollow interior space/cavity for both higher active material content and inbuilt self-supporting framework. The existence of the submicron aperture or opening on the shell of the AYs structure warrants a shorter electrode activation process since electrolyte ions can readily diffuse into the interior of the yolk–shell structures. Moreover, yolk–shell structures are created by a surfactant-induced formation mechanism, which leads to highly exposed crystal (400) facets for improved electrochemical activities. The characteristics of the physical and unique crystallography have endowed the materials with high specific capacitance with excellent cycling performance (5000 cycles) in supercapacitors and high electrocatalytic activities with good stability in water splitting.

### 4. MATERIALS AND METHODS

**Material Preparation.** The nickel cobalt (Ni-Co) precursors can be readily synthesized by a simple solvothermal method. In a typical synthesis of AYs, 0.2 mmol of  $\text{Ni}(\text{NO}_3)_2 \cdot 6\text{H}_2\text{O}$  and 0.4 mmol of  $\text{Co}(\text{NO}_3)_2 \cdot 6\text{H}_2\text{O}$  were dissolved in 25 mL of isopropanol (IPA) under

magnetic stirring at room temperature, followed by the addition of 1 mL of ethylene glycol (EG) and 0.1 g of polyvinylpyrrolidone (PVP, MW = 10 K). The solution was then transferred to a 50 mL Teflon-lined stainless steel autoclave and heated at  $180 \text{ }^\circ\text{C}$  for 6 h. The resulting precursor was then collected via centrifugation and rinsed with DI water before drying at  $60 \text{ }^\circ\text{C}$  overnight. Calcination in air at  $400 \text{ }^\circ\text{C}$  for 3 h at a heating rate of  $1 \text{ }^\circ\text{C min}^{-1}$  was then carried out to convert the precursor to  $\text{NiCo}_2\text{O}_4$ . As a comparison, a conventional SYs sample was prepared following the same procedure in the absence of PVP. Furthermore, control  $\text{NiCo}_2\text{O}_4$  solid nanoparticles spheres were also prepared following the same synthesis process without adding EG or PVP.

**Materials Characterizations.** The morphologies and crystallographic and chemical compositions of Ni-Co precursors and subsequent  $\text{NiCo}_2\text{O}_4$  samples were characterized by scanning electron microscopy (FESEM, JEOL FEG JSM-7001F) equipped with an energy-dispersive X-ray spectroscopy (EDX), X-ray diffraction (XRD, Philips X-ray diffractometer,  $\text{Cu K}\alpha$ ,  $\lambda = 1.5406 \text{ \AA}$ ), transmission electron microscopy (TEM, Philips FEG CM300 equipped with selected area electron diffraction (SAED) and element mapping attachment), and X-ray photoelectron spectroscopy (XPS, VGSCALAB 220I-XL). Thermal gravimetric analysis (TGA, DTG-60AH Shimadzu, with a heating rate of  $5 \text{ }^\circ\text{C min}^{-1}$  from RT to  $600 \text{ }^\circ\text{C}$  under  $50 \text{ mL min}^{-1}$  of air flow) was carried out to monitor the weight loss of the AYs and SYs Ni-Co precursors. The texture properties of the oxide samples were carried out at 77 K with a Quantachrome NOVA-1200 system using the Brunauer, Emmett, and Teller (BET) method.

**Evaluation of Supercapacitive Performances.** The working electrodes were prepared by mixing 80 wt % of the electroactive material ( $\text{NiCo}_2\text{O}_4$ ), 10 wt % of carbon black, and 10 wt % of polyvinylidene difluoride (PVDF, Aldrich). The slurry was then pressed onto Ni foams and dried at  $60 \text{ }^\circ\text{C}$ . The electrolyte used was a 2 M KOH aqueous solution. The electrochemical performances including cyclic voltammetry (CV), galvanostatic charge–discharge (GCCD), and electrochemical impedance spectroscopy (EIS) of the samples were evaluated on a CHI 660E electrochemical workstation with a three-electrode cell where Pt foil serves as the counter electrode and a standard calomel electrode (SCE) as the reference electrode. The asymmetrical two-electrode system was also fabricated to evaluate the electrochemical performances of the typical AYs sample, where the AYs sample and activated carbon served as the two working electrodes. The CV and GCCD measurements were performed in the potential range of 0–1 V at scan rates of  $1\text{--}20 \text{ mV s}^{-1}$  and at current densities of  $0.125\text{--}1 \text{ A g}^{-1}$ , respectively.

**Evaluation of Electrocatalytic Activity for OER.** A 10 mg portion of the active material was mixed with 0.9 mL of ethanol and 0.1 mL of 7% PVDF solution (in DMF) by sonication for 10 min. Then, the suspension was applied onto an area of  $1.5 \text{ cm}^2$  of a piece of nickel foam ( $1.5 \text{ cm} \times 3 \text{ cm}$ ). The mass loading of the active material is about 3.6 mg. The catalytic activity was measured in a three-electrode system with a CHI 660E electrochemical workstation using 1 M KOH aqueous solution as electrolyte. The Pt foil and SCE were used as counter electrode and reference electrode, respectively. All the measured potentials were referred to the reversible hydrogen electrode (RHE) with the following equation:

$$E(\text{RHE}) = E(\text{SCE}) + 1.1$$

Linear sweep voltammetry was performed at a scan rate of  $5 \text{ mV s}^{-1}$  for the polarization curves.

## ■ ASSOCIATED CONTENT

### Supporting Information

The Supporting Information is available free of charge on the ACS Publications website at DOI: 10.1021/acsami.6b12284.

SEM, TEM, EDX, XRD, TGA, BET, elemental mappings, electrochemical data, etc., of the prepared samples (PDF)

## AUTHOR INFORMATION

## Corresponding Author

\*E-mail: elehgw@nus.edu.sg.

## ORCID

Ting Zhu: 0000-0001-5567-3809

## Notes

The authors declare no competing financial interest.

## ACKNOWLEDGMENTS

This work is supported by R-263-000-B38-112 and R-263-000-B63-112 (Ministry of Education, Republic of Singapore).

## REFERENCES

- (1) Bao, J.; Zhang, X. D.; Fan, B.; Zhang, J. J.; Zhou, M.; Yang, W. L.; Hu, X.; Wang, H.; Pan, B. C.; Xie, Y. Ultrathin Spinel-Structured Nanosheets Rich in Oxygen Deficiencies for Enhanced Electrocatalytic Water Oxidation. *Angew. Chem., Int. Ed.* **2015**, *54*, 7399–7404.
- (2) Zhang, L. L.; Zhao, X. S. Carbon-Based Materials as Supercapacitor Electrodes. *Chem. Soc. Rev.* **2009**, *38*, 2520–2531.
- (3) Lai, X. Y.; Halpert, J. E.; Wang, D. Recent Advances in Micro-/Nano-Structured Hollow Spheres for Energy Applications: From Simple to Complex Systems. *Energy Environ. Sci.* **2012**, *5*, 5604–5618.
- (4) Lu, B. A.; Cao, D. X.; Wang, P.; Wang, G. L.; Gao, Y. Y. Oxygen Evolution Reaction on Ni-Substituted Co<sub>3</sub>O<sub>4</sub> Nanowire Array Electrodes. *Int. J. Hydrogen Energy* **2011**, *36*, 72–78.
- (5) Stoller, M. D.; Park, S. J.; Zhu, Y. W.; An, J. H.; Ruoff, R. S. Graphene-Based Ultracapacitors. *Nano Lett.* **2008**, *8*, 3498–3502.
- (6) Arico, A. S.; Bruce, P.; Scrosati, B.; Tarascon, J. M.; Van Schalkwijk, W. Nanostructured Materials for Advanced Energy Conversion and Storage Devices. *Nat. Mater.* **2005**, *4*, 366–377.
- (7) Kim, S. W.; Kim, M.; Lee, W. Y.; Hyeon, T. Fabrication of Hollow Palladium Spheres and Their Successful Application to the Recyclable Heterogeneous Catalyst for Suzuki Coupling Reactions. *J. Am. Chem. Soc.* **2002**, *124*, 7642–7643.
- (8) Zhou, X. M.; Xia, Z. M.; Tian, Z. M.; Ma, Y. Y.; Qu, Y. Q. Ultrathin Porous Co<sub>3</sub>O<sub>4</sub> Nanoplates as Highly Efficient Oxygen Evolution Catalysts. *J. Mater. Chem. A* **2015**, *3*, 8107–8114.
- (9) Wang, Y. C.; Zhou, T.; Jiang, K.; Da, P. M.; Peng, Z.; Tang, J.; Kong, B. A.; Cai, W. B.; Yang, Z. Q.; Zheng, G. F. Reduced Mesoporous Co<sub>3</sub>O<sub>4</sub> Nanowires as Efficient Water Oxidation Electrocatalysts and Supercapacitor Electrodes. *Adv. Energy Mater.* **2014**, *4*, 7.
- (10) Zhu, T.; Chen, J. S.; Lou, X. W. Shape-Controlled Synthesis of Porous Co<sub>3</sub>O<sub>4</sub> Nanostructures for Application in Supercapacitors. *J. Mater. Chem.* **2010**, *20*, 7015–7020.
- (11) Zhang, G. Q.; Lou, X. W. Controlled Growth of NiCo<sub>2</sub>O<sub>4</sub> Nanorods and Ultrathin Nanosheets on Carbon Nanofibers for High-Performance Supercapacitors. *Sci. Rep.* **2013**, *3*, 1470.
- (12) Lv, X. M.; Zhu, Y. H.; Jiang, H. L.; Yang, X. L.; Liu, Y. Y.; Su, Y. H.; Huang, J. F.; Yao, Y. F.; Li, C. Z. Hollow Mesoporous NiCo<sub>2</sub>O<sub>4</sub> Nanocages as Efficient Electrocatalysts for Oxygen Evolution Reaction. *Dalton Trans.* **2015**, *44*, 4148–4154.
- (13) Chen, R.; Wang, H. Y.; Miao, J. W.; Yang, H. B.; Liu, B. A Flexible High-Performance Oxygen Evolution Electrode with Three-Dimensional NiCo<sub>2</sub>O<sub>4</sub> Core-Shell Nanowires. *Nano Energy* **2015**, *11*, 333–340.
- (14) Caruso, F.; Caruso, R. A.; Mohwald, H. Nanoengineering of Inorganic and Hybrid Hollow Spheres by Colloidal Templating. *Science* **1998**, *282*, 1111–1114.
- (15) Zoldesi, C. I.; Imhof, A. Synthesis of Monodisperse Colloidal Spheres, Capsules, and Microballoons by Emulsion Templating. *Adv. Mater.* **2005**, *17*, 924–928.
- (16) Lu, A. H.; Sun, T.; Li, W. C.; Sun, Q.; Han, F.; Liu, D. H.; Guo, Y. Synthesis of Discrete and Dispersible Hollow Carbon Nanospheres with High Uniformity by Using Confined Nanospace Pyrolysis. *Angew. Chem., Int. Ed.* **2011**, *50*, 11765–11768.
- (17) Sun, J. H.; Zhang, J. S.; Zhang, M. W.; Antonietti, M.; Fu, X. Z.; Wang, X. C. Bioinspired Hollow Semiconductor Nanospheres as Photosynthetic Nanoparticles. *Nat. Commun.* **2012**, *3*, 1139.
- (18) Wan, H. R.; Long, Y.; Xu, H.; Song, K.; Yang, G. Q.; Tung, C. H. New Strategy to Prepare Hollow Silica Microspheres with Tunable Holes on the Shell Wall. *Langmuir* **2014**, *30*, 683–686.
- (19) Shao, M. F.; Ning, F. Y.; Zhao, Y. F.; Zhao, J. W.; Wei, M.; Evans, D. G.; Duan, X. Core-Shell Layered Double Hydroxide Microspheres with Tunable Interior Architecture for Supercapacitors. *Chem. Mater.* **2012**, *24*, 1192–1197.
- (20) Li, J. F.; Wang, J. Z.; Liang, X.; Zhang, Z. J.; Liu, H. K.; Qian, Y. T.; Xiong, S. L. Hollow MnCo<sub>2</sub>O<sub>4</sub> Submicrospheres with Multilevel Interiors: From Mesoporous Spheres to Yolk-in-Double-Shell Structures. *ACS Appl. Mater. Interfaces* **2014**, *6*, 24–30.
- (21) Liu, N.; Wu, H.; McDowell, M. T.; Yao, Y.; Wang, C. M.; Cui, Y. A Yolk-Shell Design for Stabilized and Scalable Li-Ion Battery Alloy Anodes. *Nano Lett.* **2012**, *12*, 3315–3321.
- (22) Liu, J.; Qiao, S. Z.; Chen, J. S.; Lou, X. W.; Xing, X. R.; Lu, G. Q. Yolk/Shell Nanoparticles: New Platforms for Nanoreactors, Drug Delivery and Lithium-Ion Batteries. *Chem. Commun.* **2011**, *47*, 12578–12591.
- (23) Liu, J.; Yang, H. Q.; Kleitz, F.; Chen, Z. G.; Yang, T. Y.; Strounina, E.; Lu, G. Q.; Qiao, S. Z. Yolk-Shell Hybrid Materials with a Periodic Mesoporous Organosilica Shell: Ideal Nanoreactors for Selective Alcohol Oxidation. *Adv. Funct. Mater.* **2012**, *22*, 591–599.
- (24) Yang, T. Y.; Liu, J.; Zheng, Y.; Monteiro, M. J.; Qiao, S. Z. Facile Fabrication of Coreshell-Structured Ag@Carbon and Mesoporous Yolkshell-Structured Ag@Carbon@Silica by an Extended Stober Method. *Chem. - Eur. J.* **2013**, *19*, 6942–6945.
- (25) Zhang, L. Q.; Qian, K.; Wang, X. P.; Zhang, F.; Shi, X.; Jiang, Y. J.; Liu, S. M.; Jaroniec, M.; Liu, J. Yolk-Shell-Structured Aluminum Phenylphosphonate Microspheres with Anionic Core and Cationic Shell. *Adv. Sci.* **2016**, *3*, 1500363.
- (26) Jiang, X. C.; Wang, Y. L.; Herricks, T.; Xia, Y. N. Ethylene Glycol-Mediated Synthesis of Metal Oxide Nanowires. *J. Mater. Chem.* **2004**, *14*, 695–703.
- (27) Niu, Z. Q.; Li, Y. D. Removal and Utilization of Capping Agents in Nanocatalysis. *Chem. Mater.* **2014**, *26*, 72–83.
- (28) Li, L. L.; Cheah, Y.; Ko, Y. W.; Teh, P.; Wee, G.; Wong, C. L.; Peng, S. J.; Srinivasan, M. The Facile Synthesis of Hierarchical Porous Flower-Like NiCo<sub>2</sub>O<sub>4</sub> with Superior Lithium Storage Properties. *J. Mater. Chem. A* **2013**, *1*, 10935–10941.
- (29) Boyjoo, Y.; Wang, M.; Pareek, V. K.; Liu, J.; Jaroniec, M. Synthesis and Applications of Porous Non-Silica Metal Oxide Submicrospheres. *Chem. Soc. Rev.* **2016**, *45*, 6013–6047.
- (30) Cui, B.; Lin, H.; Li, J. B.; Li, X.; Yang, J.; Tao, J. Core-Ring Structured NiCo<sub>2</sub>O<sub>4</sub> Nanoplatelets: Synthesis, Characterization, and Electrocatalytic Applications. *Adv. Funct. Mater.* **2008**, *18*, 1440–1447.
- (31) Somorjai, G. A.; Blakely, D. W. Mechanism of Catalysis of Hydrocarbon Reactions by Platinum Surfaces. *Nature* **1975**, *258*, 580–583.
- (32) Li, D. L.; Gong, Y. N.; Zhang, Y. P.; Luo, C. Z.; Li, W. P.; Fu, Q.; Pan, C. X. Facile Synthesis of Carbon Nanosphere/NiCo<sub>2</sub>O<sub>4</sub> Core-Shell Sub-Microspheres for High Performance Supercapacitor. *Sci. Rep.* **2015**, *5*, 12903.
- (33) Yuan, C. Z.; Li, J. Y.; Hou, L. R.; Zhang, X. G.; Shen, L. F.; Lou, X. W. Ultrathin Mesoporous NiCo<sub>2</sub>O<sub>4</sub> Nanosheets Supported on Ni Foam as Advanced Electrodes for Supercapacitors. *Adv. Funct. Mater.* **2012**, *22*, 4592–4597.
- (34) Xia, Y. N.; Xiong, Y. J.; Lim, B.; Skrabalak, S. E. Shape-Controlled Synthesis of Metal Nanocrystals: Simple Chemistry Meets Complex Physics? *Angew. Chem., Int. Ed.* **2009**, *48*, 60–103.
- (35) Anderson, B. D.; Tracy, J. B. Nanoparticle Conversion Chemistry: Kirkendall Effect, Galvanic Exchange, and Anion Exchange. *Nanoscale* **2014**, *6*, 12195–12216.
- (36) Fan, H. J.; Knez, M.; Scholz, R.; Hesse, D.; Nielsch, K.; Zacharias, M.; Gosele, U. Influence of Surface Diffusion on the Formation of Hollow Nanostructures Induced by the Kirkendall Effect: The Basic Concept. *Nano Lett.* **2007**, *7*, 993–997.

(37) Zhang, G. Q.; Lou, X. W. General Solution Growth of Mesoporous NiCo<sub>2</sub>O<sub>4</sub> Nanosheets on Various Conductive Substrates as High-Performance Electrodes for Supercapacitors. *Adv. Mater.* **2013**, *25*, 976–979.

(38) Liu, X. Y.; Zhang, Y. Q.; Xia, X. H.; Shi, S. J.; Lu, Y.; Wang, X. L.; Gu, C. D.; Tu, J. P. Self-Assembled Porous NiCo<sub>2</sub>O<sub>4</sub> Hetero-Structure Array for Electrochemical Capacitor. *J. Power Sources* **2013**, *239*, 157–163.

(39) Zhou, W. W.; Kong, D. Z.; Jia, X. T.; Ding, C. Y.; Cheng, C. W.; Wen, G. W. NiCo<sub>2</sub>O<sub>4</sub> Nanosheet Supported Hierarchical Core-Shell Arrays for High-Performance Supercapacitors. *J. Mater. Chem. A* **2014**, *2*, 6310–6315.

(40) An, C. H.; Wang, Y. J.; Huang, Y. A.; Xu, Y. A.; Xu, C. C.; Jiao, L. F.; Yuan, H. T. Novel Three-Dimensional NiCo<sub>2</sub>O<sub>4</sub> Hierarchitectures: Solvothermal Synthesis and Electrochemical Properties. *CrystEngComm* **2014**, *16*, 385–392.

(41) Kong, D. Z.; Ren, W. N.; Cheng, C. W.; Wang, Y.; Huang, Z. X.; Yang, H. Y. Three-Dimensional NiCo<sub>2</sub>O<sub>4</sub>@Polypyrrole Coaxial Nanowire Arrays on Carbon Textiles for High-Performance Flexible Asymmetric Solid-State Supercapacitor. *ACS Appl. Mater. Interfaces* **2015**, *7*, 21334–21346.

(42) Hu, H.; Guan, B. Y.; Xia, B. Y.; Lou, X. W. Designed Formation of Co<sub>3</sub>O<sub>4</sub>/NiCo<sub>2</sub>O<sub>4</sub> Double-Shelled Nanocages with Enhanced Pseudocapacitive and Electrocatalytic Properties. *J. Am. Chem. Soc.* **2015**, *137*, 5590–5595.

(43) Yin, J.; Zhou, P. P.; An, L.; Huang, L.; Shao, C. W.; Wang, J.; Liu, H. Y.; Xi, P. X. Self-Supported Nanoporous NiCo<sub>2</sub>O<sub>4</sub> Nanowires with Cobalt-Nickel Layered Oxide Nanosheets for Overall Water Splitting. *Nanoscale* **2016**, *8*, 1390–1400.

(44) McCrory, C. C. L.; Jung, S. H.; Peters, J. C.; Jaramillo, T. F. Benchmarking Heterogeneous Electrocatalysts for the Oxygen Evolution Reaction. *J. Am. Chem. Soc.* **2013**, *135*, 16977–16987.